PNAS
www.pnas.org

Supplementary Information for

Enhanced mixing across the gyre boundary at the Gulf Stream front

Jacob O. Wenegrat, Leif. N. Thomas, Miles A. Sundermeyer, John R. Taylor, Eric A. D'Asaro, Jody M. Klymak, R. Kipp Shearman, and Craig M. Lee

Jacob O. Wenegrat
E-mail: wenegrat@umd.edu

This PDF file includes:

Supplementary text
Figs. S1 to S4
Legends for Movies S1 to S2
SI References

Other supplementary materials for this manuscript include the following:

Movies S1 to S2

www.pnas.org/cgi/doi/10.1073/pnas.2005558117

Supporting Information Text

Calculation of effective horizontal diffusivity

The high-resolution cross-frontal surveys taken from the *R/V Knorr* allow the dye evolution to be quantified in time (figure S1). To calculate the effective horizontal diffusivity of the dye, each cross-frontal survey is gridded to uniform bins in the cross-frontal and vertical direction, and treated as a discrete observation in time. The cross-frontal variance of the dye is then calculated at each time and depth level as,

$$\sigma_y^2(z,t) = \frac{\int_{y_l}^{y_r} \left[y - y_{COM}(z,t)\right]^2 C(y,z,t)\mathrm{dy}}{\int_{y_l}^{y_r} C(y,z,t)\mathrm{dy}}, \qquad [1]$$

where y_l and y_r are the horizontal limits of each cross-frontal survey, y_{COM} is the cross-frontal position of the dye center of mass, and $C(y,z,t)$ is the dye concentration. The horizontally averaged vertical variance is also calculated,

$$\sigma_z^2(t) = \frac{\int_{z_b}^{0} \left[z - z_{COM}(t)\right]^2 \langle C\rangle \mathrm{dz}}{\int_{z_b}^{0} \langle C\rangle \mathrm{dz}}, \qquad [2]$$

where z_b is the deepest observational bin, z_{COM} is the vertical center of mass of $\langle C\rangle$, and bracket notation indicates averaging horizontally over a survey. A concentration-weighted vertical average of the cross-frontal variance is then calculated as,

$$\overline{\sigma_y^2(t)} = \frac{\int_{z_m}^{z_p} \sigma_y^2(z,t)\langle C\rangle \mathrm{dz}}{\int_{z_m}^{z_p} \langle C\rangle \mathrm{dz}}, \qquad [3]$$

restricted to depth ranges within $\pm 2\sigma_z$ of the vertical center of mass at each time. This approach reduces noise associated with depth ranges with very low observed dye concentrations.

To determine the effective horizontal diffusivity based on dye observations taken in 2D transects across the front, it is necessary to account for unresolved along-front variability in the dye patch which can be generated by the vertical and across front shear of the along-front flow (ie. $\partial u/\partial z$ and $\partial u/\partial y$). To do this we assume that the 3D dye patch evolves according to a standard advection-diffusion equation (1),

$$\frac{\partial C}{\partial t} + u\frac{\partial C}{\partial x} = \kappa_z \frac{\partial^2 C}{\partial z^2} + \kappa_h \left(\frac{\partial^2}{\partial x^2} + \frac{\partial^2}{\partial y^2}\right) C, \qquad [4]$$

where κ_z is the vertical diffusivity, and for simplicity it is assumed $u = (5\times 10^{-3}s^{-1})z - (5\times 10^{-5}s^{-1})y$ (with values determined from shipboard ADCP observations around the dye center of mass). From this model all 9 moments of the 3D dye patch are computed, and then the y-moments of the tracer are evaluated to determine the effective cross-stream moments that would be observed in a single 2D cross-stream (y-z) transect through the center of the 3D patch. The model free parameters, κ_z and κ_h, are then chosen to best fit the observed cross-frontal dye variance from the ship transects ($\kappa_z \approx 10^{-2}$ $\mathrm{m^2s^{-1}}$ and $\kappa_h \approx 50$ $\mathrm{m^2s^{-1}}$).

For the numerical simulations, the modeled tracer is first integrated in the along-front direction, and then the horizontal center of mass is calculated by projecting the periodic cross-frontal direction to a circular coordinate system, with angle,

$$\theta_{COM}(z,t) = Arg\left[\int_0^{2\pi} C(\theta,z,t)e^{i\theta}\mathrm{d}\theta\right], \qquad [5]$$

where $\theta = 2\pi y/L_y$. This angle is then used to center the dye patch in the periodic domain, as a function of depth-level and time-step. The calculation of the dye variance then follows the steps outlined above. This approach minimizes the effect of wrapping of the dye around the periodic domain, however we note that as the horizontal standard deviation of the dye patch becomes comparable to the domain size wrapping effects become unavoidable. Assuming a dye patch that remains Gaussian, wrapping of the dye patch will tend to bias the numerical model estimates of the increase of variance, and hence diffusivity, low.

The model dye concentrations are integrated in the along-front (x) direction, hence an estimate of the effective horizontal diffusivity for the numerical simulations can be formed directly from the increase in the cross-frontal variance as,

$$\frac{\partial \overline{\sigma_y^2}}{\partial t} = 2\kappa_h. \qquad [6]$$

Configuration of the numerical model

Numerical simulations are performed using the nonhydrostatic Diablo Large-Eddy Simulation (LES) code (2). The numerical configuration closely follows that described in (3), but uses a larger domain in the cross-frontal direction to allow for the horizontal dye dispersion. The domain used here has size (L_x, L_y, L_z) = (500 m, 10 km, 150 m), with uniform resolution of 3.9 m in both horizontal directions, and vertical resolution ranging between $0.9 - 1.9$ m with enhanced resolution near the surface. This resolution is sufficient to resolve the largest of the turbulent eddies, and subgrid-scale fluxes are modeled using a

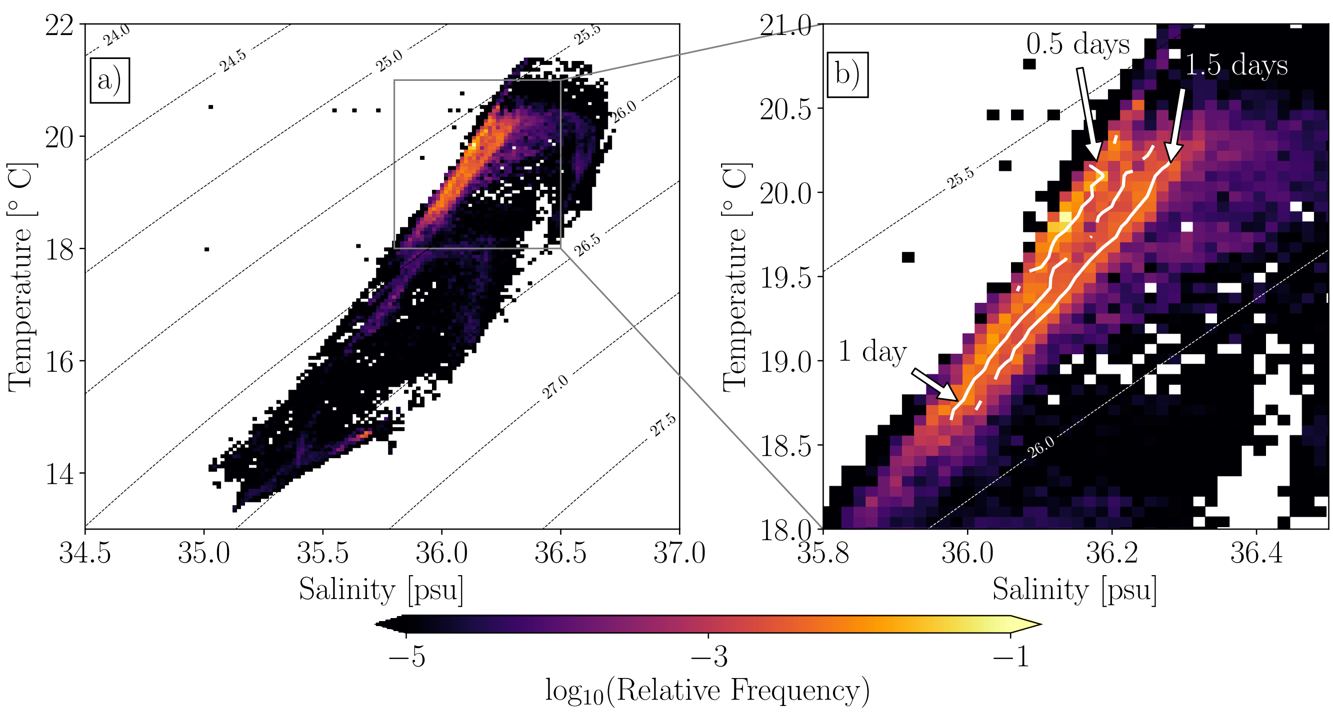

Fig. S1. Evolution of the dye from the *R/V Knorr* observations in temperature-salinity space. a) Joint histogram of the dye observations in temperature-salinity space, weighted by the observed concentration (color). Sigma (density) surfaces are shown for reference (dashed contours, with units of kg m^{-3}). b) As in panel a, enlarging the region of highest relative frequency, as indicated. Also shown are contours of the concentration-weighted average yearday associated with the observations in each bin (white, restricted to regions with relative frequency greater than 10^{-3}) with labels indicating elapsed time from the dye release.

modified Smagorinsky closure. Both horizontal directions are periodic, and the vertical direction is bounded with rigid lids on either end of the domain. An additional sponge layer is added near the bottom of the domain to reduce wave reflection. The dye undergoes less horizontal dispersion in the NO-FRONT and NO-GEOMIX simulations, and therefore in the interest of computational efficiency these runs were performed with a reduced domain size in the y-direction of 5 km. Passive tracer diffusion assumes a subgrid diffusivity equal to that of buoyancy. Additional details of the numerical method are provided in (2), and (3).

Simulations FRONT and NO-GEOMIX are run in a 'frontal-zone' configuration, a common approach to modeling surface boundary layer fronts when using spectral methods which require horizontal periodicity (3, 4). In this setup a steady, spatially-uniform and geostrophically-balanced, background horizontal buoyancy gradient is imposed. Solutions are then found for velocity and buoyancy perturbations away from the balanced background state. The equations solved are given by,

$$\frac{\partial \mathbf{u}}{\partial t} + \left(\mathbf{u} + u_g\hat{i}\right)\cdot\nabla\mathbf{u} + \underbrace{w\frac{\partial u_g}{\partial z}\hat{i}}_{GEOMIX} + f\hat{k}\times\mathbf{u} = -\frac{1}{\rho_o}\nabla p + b\hat{k} + \nu\nabla^2\mathbf{u} + \mathbf{F}_{sgs}, \qquad [7]$$

and

$$\frac{\partial b}{\partial t} + \left(\mathbf{u} + u_g\hat{i}\right)\cdot\nabla b + v\frac{\partial \bar{b}}{\partial y} = \kappa\nabla^2 b + B_{sgs}, \qquad [8]$$

$$\nabla\cdot\mathbf{u} = 0. \qquad [9]$$

In the above, $\mathbf{u} = (u\hat{i}, v\hat{j}, w\hat{k})$ is the perturbation velocity vector, f is the Coriolis frequency, ρ_o is a constant background density, p is the perturbation pressure, b is the perturbation buoyancy, ν (κ) is the molecular viscosity (diffusivity), and $\mathbf{F}_{sgs}$ (B_{sgs}) is the subgrid momentum (buoyancy) flux convergence. The geostrophically balanced background flow, u_g, is a function of only the vertical direction, and is found by integrating the thermal wind balance vertically from the bottom of the domain ($\partial u_g/\partial z = -f^{-1}\partial\bar{b}/\partial y$). In the NO-GEOMIX experiment the GEOMIX term is set to zero, removing vertical advection of the geostrophic momentum. This suppresses both the turbulent mixing of the thermal wind shear and the development of symmetric instability, which grows through vertical fluxes that extract background kinetic energy via the thermal wind shear (5). Note however that in this configuration advection of the background buoyancy gradient still influences the evolution of the buoyancy field, allowing the presence of the front to influence the structure of the boundary layer (unlike in the NO-FRONT run).

Generation of cross-frontal shear

A detailed analysis of the dynamics leading to the explosive growth of SI during these observations is given in (3). Here we focus on the generation mechanism for the cross-frontal shear, as this plays a central role in causing the shear dispersion that is the focus of this manuscript. The importance of the mixing of geostrophic momentum is immediately evident in comparing the evolution of the NO-GEOMIX and FRONT simulations, as this is the primary difference between the configurations (the domain size also differs but was tested and found to not effect the dynamical evolution). Critically, while in both simulations an inertial oscillation is generated (figure S2), in the NO-GEOMIX run this oscillation has little vertical shear. The dye patch in NO-GEOMIX therefore undergoes little shear-dispersion, and the cross-frontal variance grows at a rate comparable to the NO-FRONT run (figure 5). This numerical experiment, and the results of the NO-FRONT run, thus confirm that mixing of geostrophic momentum is necessary for the generation of the cross-frontal shear flow, and subsequent shear dispersion, evident in the FRONT simulation.

The steady-state dynamics of how turbulent mixing in the presence of a horizontal buoyancy gradient leads to cross-frontal shear have been discussed recently in (6), and time-dependent solutions for the coupled evolution between the velocity field and buoyancy field are provided in (7), and (8), assuming idealized models for the turbulent viscosity and diffusivity. However, a simple demonstration of how the mixing of geostrophic momentum generates a time-dependent cross-frontal shear can be given by horizontally averaging the ageostrophic component of the horizontal momentum equations,

$$\frac{\partial\langle u\rangle}{\partial t} - f\langle v\rangle = -\frac{\partial\langle w'u'\rangle}{\partial z}, \qquad [10]$$

$$\frac{\partial\langle v\rangle}{\partial t} + f\langle u\rangle = -\frac{\partial\langle w'v'\rangle}{\partial z}, \qquad [11]$$

where $\langle\cdot\rangle$ indicates horizontal averaging, primes indicate departure from the horizontal average, and molecular and subgrid-scale turbulent fluxes are neglected as they are important only very near the boundaries. Note that horizontal convergence terms do not appear as the domain is horizontally periodic.

Now, assume a flow initially in geostrophic balance (ie. the initial perturbation velocities are $u_o = v_o = 0$) that is subjected to a steady forcing that generates turbulence, such that the flow adjusts towards some new equilibrium balance, with ageostrophic component satisfying,

$$-f\langle v\rangle_{eq} = -\frac{\partial\langle w'u'\rangle_{eq}}{\partial z}, \qquad [12]$$

$$f\langle u\rangle_{eq} = -\frac{\partial\langle w'v'\rangle_{eq}}{\partial z}. \qquad [13]$$

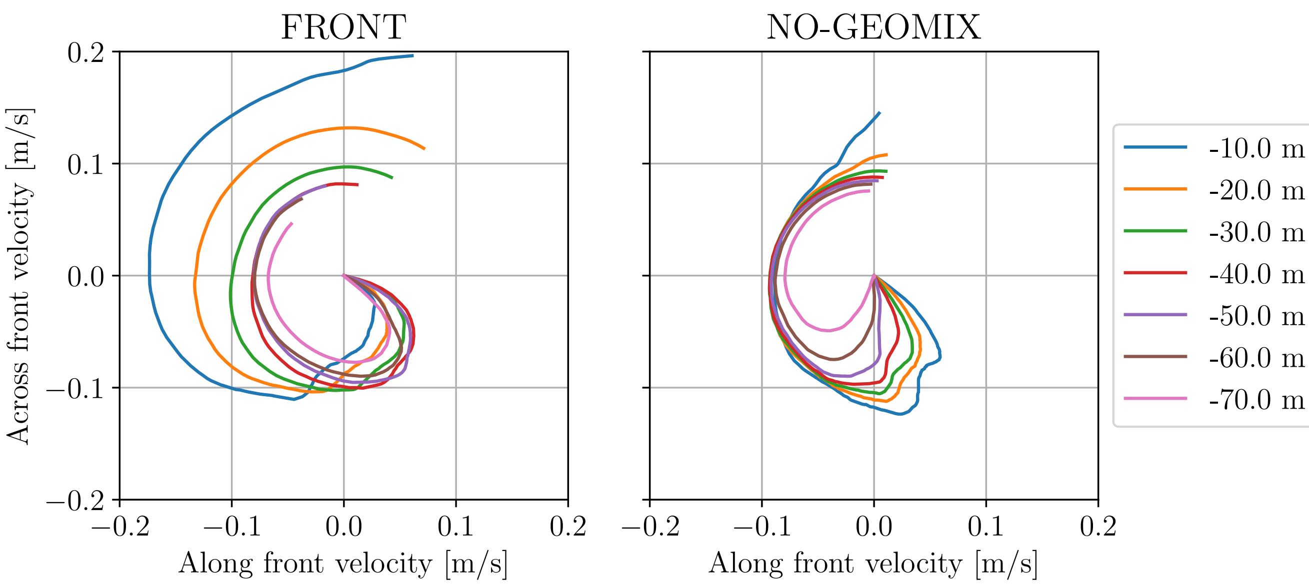

Fig. S2. Hodographs of horizontally averaged perturbation velocity (ie. the departure from the geostrophic background flow) for the FRONT and NO-GEOMIX runs. Values are plotted at various depths (as indicated in the legend) for a time span beginning at model initialization (yearday 64.5) and ending just prior to the strong wind forcing (yearday 65.2).

In general the details of this adjustment process will be complex (see for example (7, 8)), however the basic outcome can be very simply illustrated by assuming that the right-hand side terms of [10] and [11] can be replaced by their equilibrium values given in [12] and [13]. Discussion of the physical interpretation of this simplification, applied to a different problem setting, can be found in (9). Using this assumption, and the definition of the equilibrium solution, the equations can then be written as,

$$\frac{\partial}{\partial t}\left(\langle u\rangle - \langle u\rangle_{eq}\right) - f(\langle v\rangle - \langle v\rangle_{eq}) = 0, \qquad [14]$$

$$\frac{\partial}{\partial t}\left(\langle v\rangle - \langle v\rangle_{eq}\right) + f(\langle u\rangle - \langle u\rangle_{eq}) = 0. \qquad [15]$$

Which has solutions (9),

$$\langle u\rangle - \langle u\rangle_{eq} = -\langle v_{eq}\rangle \sin(ft) - \langle u_{eq}\rangle \cos(ft), \qquad [16]$$

$$\langle v\rangle - \langle v\rangle_{eq} = -\langle v_{eq}\rangle \cos(ft) + \langle u_{eq}\rangle \sin(ft). \qquad [17]$$

The total velocity field thus describes oscillations at the inertial frequency around the total equilibrium solution, $(\langle u_{eq}\rangle + u_g, \langle v_{eq}\rangle)$, with the envelope of the oscillations given by the difference between the total equilibrium solution and the initial geostrophically balanced flow,

$$\langle u_T\rangle = \langle u\rangle + u_g = u_g - \langle v_{eq}\rangle \sin(ft) + \langle u_{eq}\rangle \left[1 - \cos(ft)\right], \qquad [18]$$

$$\langle v_T\rangle = \langle v\rangle = \langle v_{eq}\rangle \left[1 - \cos(ft)\right] + \langle u_{eq}\rangle \sin(ft). \qquad [19]$$

Thus, mixing that tends to homogenizes the vertical profile of the velocity field will generate sheared inertial oscillations. A schematic of this is shown in figure S3, assuming an equilibrium profile that is uniform in the vertical, as for instance in an idealized surface mixed-layer. The oscillations evident in figure S2, and the cross-frontal flow in FRONT, can thus be understood as a response to homogenization of the vertically-sheared geostrophic velocity profile (figure 4, profiles). A final important point is that the flux terms on the right-hand side of [10] and [11], which homogenize the velocity profile, can be caused by atmospheric forcing that generates turbulence, but also by the coherent overturning motions of the SI modes and associated secondary instabilities. Submesoscale fronts, where thermal wind shears are large and these instabilities are most often found, are thus particularly susceptible to the generation of sheared inertial oscillations and the accompanying shear dispersion of tracers.

Estimate of effective tracer flux

The cross-frontal flux of a scalar quantity, χ, due to shear dispersion is estimated using the scaling $\kappa_h D \Delta\chi / L$, where κ_h is an estimate of the effective horizontal diffusivity, D the depth of the mixed-layer, $\Delta\chi$ is the change of χ across the front, and L a characteristic horizontal length scale. In the interest of simplicity we make the assumption that the diffusivity can be scaled with the observational estimate ($\kappa_h \approx 50$ m^2 s^{-1}). This is however based on a tracer release preceding a strong wind-forcing event by approximately 12 hours, whereas such wind forcing events might more generally be expected to occur on synoptic time-scales of approximately a week during wintertime in the North Atlantic. The effect of this intermittency on the effective diffusivity generated by shear dispersion will depend on whether the underlying shear flow is oscillatory or steady. In the case of oscillatory shear flow, a reduced frequency of vertical mixing events will tend to reduce the effective horizontal diffusivity (10). However, in the case of steady across-front shear flow, reducing the frequency of strong vertical mixing events will enhance horizontal dispersion (11). For the particular case studied here the shear flow appears largely oscillatory, although the presence of SI and mixing of geostrophic momentum will also tend to drive a sub-inertial component of the across-front shear flow (5, 6). As the partitioning of the total shear between oscillatory and steady components observed here is unlikely to be generally representative, and given the considerable uncertainty in the other terms in the estimate of cross-frontal flux, we proceed using the simple time-averaged estimate of the diffusivity. While beyond the scope of the present work, we also note that the scalings of (10) and (12), for oscillatory and subinertial flows respectively, both give estimates of the effective diffusivity that are roughly consistent with the observations. Specifically equation [7] of (10) predicts $\kappa_h \approx 20$ m^2 s^{-1} (using $\kappa_z = 10^{-2}$ m^2 s^{-1} and assuming the oscillatory shear scales with $\partial u_g/\partial z$) and equation [2.4] of (12) estimates $\kappa_h \approx 40$ m^2 s^{-1} (using $|\partial\bar{b}/\partial y| = 5 \times 10^{-7}$ s^{-2}, a mixed-layer depth of 100 m, and assuming heat and momentum are mixed with a timescale of 1 day).

As an example of the possible nutrient flux implied by the observed tracer dispersion it is informative to consider the flux of excess phosphate, defined as the additional phosphate available beyond the biological nitrate requirement ($P^* = PO_4^{3-} - NO_3^-/16$). The gradient in excess phosphate can be estimated from observations taken during the CLIvar MOde Water Dynamics Experiment (CLIMODE)(13). Example sections across the Gulf Stream front are shown in figure S4, from which we estimate a cross front change in $\Delta P^* \approx 0.06$ mmol m^{-3} over a length scale of approximately 5 km, consistent with (14). Note that the limited horizontal resolution of the data may bias the estimated P^* gradient low, and in particular the sharp transition in watermass properties across the Gulf Stream evident in high-resolution transects (for example the salinity section shown in figure 1) suggests the true submesoscale gradient in P^* may be significantly larger than the estimate we use here. It is not currently known how common the conditions observed in this study are along the Gulf Stream front, however they are likely more prevalent during winter, when strong winds and surface buoyancy loss generate conditions conducive to SI. Assuming, as an upper-bound, that similar conditions are found approximately half the time, shear dispersion in the mixed-layer of the Gulf Stream front (assumed here to be 3000 km in length for direct comparison with (14)) may provide as

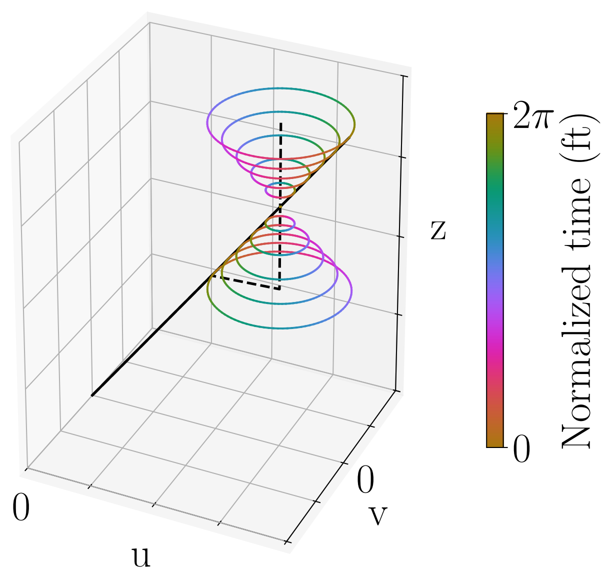

Fig. S3. Schematic of how vertical mixing of a flow, initially in thermal wind balance, can generate sheared inertial oscillations. The initial geostrophic shear flow, u_g is shown in solid black. Turbulent mixing attempts to homogenize the velocity profile in the near-surface layer, leading to an equilibrium solution $u_g + \langle u_{eq} \rangle$ shown in dashed black. Through (16) and (18) the time-dependent response will include inertial oscillations around the equilibrium solution, with envelope set by the magnitude of u_{eq}. These are depicted here at several depth levels with lines colored by time normalized by the Coriolis frequency. This schematic is based in part on figure 3 of (9).

much as 2.8×10^9 mol P^* year^{-1} to the surface mixed-layer P^* budget in the North Atlantic subtropical gyre. This value is comparable in magnitude to mechanisms such as Ekman transport and eddy stirring, believed to be important for the supply of P^* to the subtropical gyre (14, 15). However, as discussed in the manuscript, the full trajectories of fluid parcels mixed across the Gulf Stream front are currently unknown.

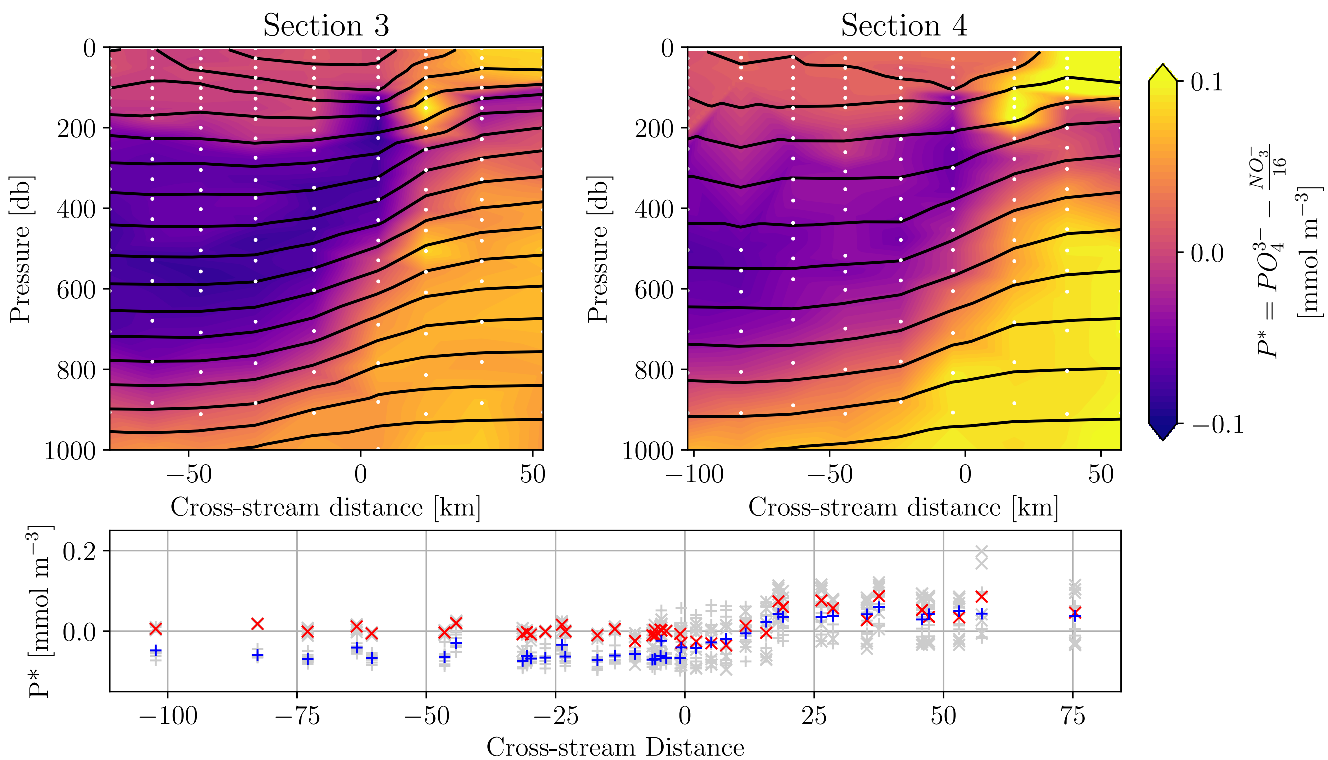

Fig. S4. Top row: Excess phosphate (colorscale), $P^* = PO_4^{3-} - NO_3^-/16$, observed across the Gulf Stream front during the CLIMODE 2006 survey sections 3 and 4 (as indicated on figure 2 of (14)), with density field (black contours), and CTD sampling locations (white dots). Bottom: CLIMODE P^* from sections 1-4 (14), averaged over the upper 200 db (red $\times$) and between 200-800 db (blue $+$). The observational scatter is indicated in grey. In all plots the cross-stream distance is calculated from the along survey distance normalized to the position and direction of the maximum depth-averaged velocity.

Movie S1. Cross-stream transects of observed dye concentration (color) and density (white contours, with interval 0.1 kg m^{-3}, and labels showing every other value of $\sigma = \rho - 1000$ kg m^{-3}). The cross-frontal distance is defined orthogonal to the Lagrangian float's direction of travel, with distance relative to the position of the float. Concentrations are normalized to the maximum observed concentration across all surveys. The bottom left panel shows the net surface heat flux (red) and wind-stress vectors (black) calculated from shipboard observations. The stress vectors are shown in a coordinate system defined by the maximum depth-integrated currents, such that downstream is parallel, and cross-stream is orthogonal, to the Gulf Stream jet (as shown in the annotation). The time span of the current ship-section is highlighted in blue. The bottom right panel shows the ship transects superimposed on a satellite SST observation (as in figure 1), with active section indicated in dashed white.

Movie S2. Animation of the passive numerical tracer (color) in the LES FRONT run, with contours of buoyancy (white, with interval equivalent to a change in density of 0.1 kg m^{-3}). The bottom panel shows the net surface heat flux (red) and wind-stress vectors (black) calculated from shipboard observations. The stress vectors are shown in a coordinate system defined by the maximum depth-integrated currents, such that downstream is parallel, and cross-stream is orthogonal, to the Gulf Stream jet (as shown in the annotation). The current yearday is indicated by the vertical dashed line.

References

1. MA Sundermeyer, JR Ledwell, Lateral dispersion over the continental shelf: Analysis of dye release experiments. *J. Geophys. Res. Ocean.* **106**, 9603–9621 (2001).
2. JR Taylor, Ph.D. Thesis (University of California, San Diego) (2008).
3. LN Thomas, et al., Symmetric Instability, Inertial Oscillations, and Turbulence at the Gulf Stream Front. *J. Phys. Oceanogr.* **46**, 197–217 (2016).
4. LN Thomas, JR Taylor, Reduction of the usable wind-work on the general circulation by forced symmetric instability. *Geophys. Res. Lett.* **37**, n/a–n/a (2010).
5. JR Taylor, R Ferrari, Buoyancy and Wind-Driven Convection at Mixed Layer Density Fronts. *J. Phys. Oceanogr.* **40**, 1222–1242 (2010).
6. JO Wenegrat, MJ McPhaden, Wind, Waves, and Fronts: Frictional Effects in a Generalized Ekman Model. *J. Phys. Oceanogr.* **46**, 371–394 (2016).
7. MN Crowe, JR Taylor, The evolution of a front in turbulent thermal wind balance. Part 1. Theory. *J. Fluid Mech.* **850**, 179–211 (2018).
8. JO Wenegrat, LN Thomas, J Gula, JC McWilliams, Effects of the Submesoscale on the Potential Vorticity Budget of Ocean Mode Waters. *J. Phys. Oceanogr.* **48**, 2141–2165 (2018).
9. BJH Van de Wiel, et al., A Conceptual View on Inertial Oscillations and Nocturnal Low-Level Jets. *J. Atmospheric Sci.* **67**, 2679–2689 (2010).
10. WR Young, PB Rhines, CJR Garrett, Shear-Flow Dispersion, Internal Waves and Horizontal Mixing in the Ocean. *J. Phys. Oceanogr.* **12**, 515–527 (1982).
11. R Ferrari, WR Young, On the development of thermohaline correlations as a result of nonlinear diffusive parameterizations. *J. Mar. Res.* **55**, 1069–1101 (1997).
12. L Chen, WR Young, Density compensated thermohaline gradients and diapycnal fluxes in the mixed layer. *J. Phys. Oceanogr.* **25**, 3064–3075 (1995).
13. The Climode Group:, et al., The Climode Field Campaign: Observing the Cycle of Convection and Restratification over the Gulf Stream. *Bull. Am. Meteorol. Soc.* **90**, 1337–1350 (2009).
14. JB Palter, MS Lozier, JL Sarmiento, RG Williams, The supply of excess phosphate across the Gulf Stream and the maintenance of subtropical nitrogen fixation. *Glob. Biogeochem. Cycles* **25**, n/a–n/a (2011).
15. RT Letscher, F Primeau, JK Moore, Nutrient budgets in the subtropical ocean gyres dominated by lateral transport. *Nat. Geosci.* **9**, 815–819 (2016).